

The impacts of vegetation on the soil surface freezing-thawing processes at permafrost southern edge simulated by an improved process-based ecosystem model

Zhenhai Liu^a, Bin Chen^{b,*}, Shaoqiang Wang^{a,b,c,*}, Qinyi Wang^a, Jinghua Chen^{b,c}, Weibo Shi^a, Xiaobo Wang^{b,c}, Yuanyuan Liu^{b,c}, Yongkai Tu^a, Mei Huang^{b,c}, Junbang Wang^{b,c}, Zhaosheng Wang^{b,c}, Hui Li^a, Tongtong Zhu^a

^a Key Laboratory of Regional Ecology and Environmental Change, School of Geography and Information Engineering, China University of Geosciences, Wuhan 430074, China

^b Key Laboratory of Ecosystem Network Observation and Modeling, Institute of Geographic Sciences and Natural Resources Research, Chinese Academy of Sciences, Beijing 100101, China

^c College of Resources and Environment, University of Chinese Academy of Sciences, Beijing, China

ARTICLE INFO

Keywords:
Freeze-thaw
Vegetation
Model improvement
Soil temperature

ABSTRACT

Permafrost degradation due to climate warming would potentially increase the release of previously frozen soil carbon and change the carbon budget of the cold region ecosystem. The underlying permafrost degradation would be effectively mediated by soil surface freezing-thawing (FT) processes. Aboveground vegetation can regulate soil FT processes, however its effects on ground thermal transfer have not been well represented by ecosystem models. In this study, we improved the hydrothermal module of the Boreal Ecosystem Productivity Simulator (BEPS) through more careful parameterization of snowpack density, puddled water, soil organic matter and super-cooled soil water. The impacts of vegetation on the soil surface FT processes have also been investigated using the improved BEPS model and the measured soil temperature data at forest and grassland sites on the southern edge of permafrost region in Mongolia and northeastern China. The improved BEPS model performs better than the original model in simulations of soil temperature and soil FT processes. Smaller amplitudes of soil diurnal FT cycles were found in forest sites compared to grassland sites. Forest sites have delayed soil thaw timing and similar soil freezing time compared to grassland sites. Differences in snow depths and soil organic matter content due to distinct vegetation community structures have considerable influences on the disparity in soil FT processes. Thus, it is important to improve the simulation of the impacts of vegetation on soil surface FT processes for better forecasting the permafrost degradation.

1. Introduction

Permafrost (the ground that remains below 0 °C for at least two consecutive years) underlies approximately 23.9% of the exposed land surface of the Northern Hemisphere and it contains twice as much carbon as the atmosphere (Grosse et al., 2016; Schädel et al., 2016). The large quantities of carbon stored in the frozen soil could be released into the atmosphere due to permafrost degradation caused by climatic warming. This degradation would potentially change the global carbon budget and accelerate global climate warming (Chaudhary et al., 2020; Hollesen et al., 2011). The most dramatic permafrost degradation

mainly occurs at the southern edge of permafrost area due to the significant poleward movement of permafrost caused by climate warming (Guo et al., 2018; Yue et al., 2020). The soil surface freezing-thawing (FT) processes, which are measured by the amplitude and duration of the diurnal soil FT cycle as well as seasonal FT timing, would effectively mediate the underlying permafrost degradation (Guo et al., 2018). The soil FT processes during the transition period from cold-to-warm or warm-to-cold seasons can last from a few days to a few weeks and they are susceptible to change because of the rapid climate warming (Bao et al., 2021; Pachauri et al., 2014).

There have been many researches investigating the soil FT processes

* Corresponding author.

E-mail addresses: chenbin@igsnrr.ac.cn (B. Chen), sqwang@igsnrr.ac.cn (S. Wang).

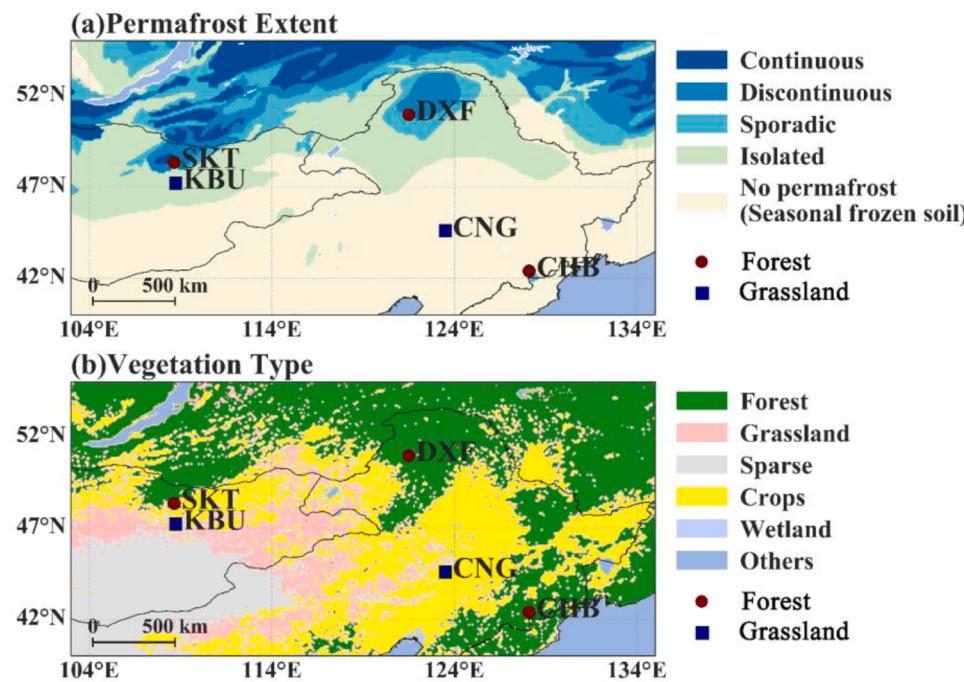


Fig. 1. (a) The permafrost extent map categorized by five types on the southern edge of east Eurasia; (b) spatial distribution of vegetation type underlying GLCNMO2013 (Kobayashi et al., 2017). The map of permafrost type, i.e., continuous (90~100%), discontinuous (50~90%), sporadic (10~50%), isolated patches (0~10%), and others (seasonally frozen soil, glacier, or water body), is obtained from the National Snow and Ice Data Center (Brown et al., 2002). Maroon and blue dots represent the locations of forest and grassland sites investigated in this study, respectively.

in response to climatic warming, mainly using near-surface soil temperature data from in situ measurements (Bao et al., 2021; Cao et al., 2020; Wang et al., 2020; Yoshikawa et al., 2020), land surface temperature data from satellites (Baltzer et al., 2014; Kim et al., 2014) as well as ecosystem model simulations (Foster et al., 2019; Guo and Wang, 2014). However, there are still uncertainties in these studies due to the sparse and short-term field measurements (Tao et al., 2017), coarse resolution of the available remote sensing data (Grosse et al., 2016; Tao et al., 2017) or the poor representation of soil FT processes in ecosystem models (Barman and Jain, 2016; Jan et al., 2020; Nitzbon et al., 2020). To better understand the pattern and drivers of the soil FT processes at regional scale, the more realistic representation and parameterizations of soil FT processes are needed to be incorporated into ecosystem models.

The impacts of vegetation on soil FT processes have been examined by many studies. Field measurements in south Siberia (Hu et al., 2013), Zhangbei county of Hebei province, China (Chen et al., 2020) and Qinghai-Tibetan Plateau (Hu et al., 2020a) found that vegetation could exert buffer effect on soil temperature, and consequently affect the soil FT processes. Guo et al. (2018) found that soil FT cycles would be larger in amplitude and longer in duration at steppe sites than at forest sites. Soils in the forest sites and steppe sites froze almost simultaneously, but experience a delay in thawing for forest sites (Guo et al., 2018). In addition, the hydrologic and thermal regimes of soil surface and soil FT processes could be affected by vegetation through intercepting snowfall and solar radiation (Chang et al., 2015; French, 2007; Karjalainen et al., 2019) and through buffer effect of litter layer (Chaudhary et al., 2020; Lawrence and Slater, 2008). Thus, it is essential to improve the ecosystem model for better simulating the impacts of vegetation on soil FT processes.

Three forest sites and two grassland sites investigated in this study were located along a vast latitudinal (around 10°) and longitudinal (around 20°) gradient at the south edge of the permafrost region of Mongolia and northeastern China. Soil temperature and meteorological data were recorded at these sites during 2003 to 2014. The soil-vegetation thermal and hydraulic modules of the Boreal Ecosystems Productivity Simulator (BEPS) have been improved and tested at the studied sites. Using the measured soil temperature data and those simulated by the BEPS model, we investigated the impacts of vegetation

types on soil FT processes.

2. Materials and methods

2.1. Site description

Three forest and two grassland sites at the southern edge of a permafrost region in Mongolia and northeastern China were investigated in this study (Fig. 1 and Table 1). Three sites (SKT, DXF, and KBU) are in the permafrost region, and two sites (CHB and CNG) belong to the region of seasonally frozen ground. These sites were selected fulfilling the following conditions in data quality and availability: (1) soil data including soil texture and soil organic carbon (SOC) content are available; (2) two or more years of continuous hourly measurements of soil temperature and meteorological variables, including air temperature, downward shortwave radiation, relative humidity, precipitation, and wind speed are available; (3) ground measurements of leaf area index (LAI) and clumping index are available. Table S1 shows the detailed information about these observational items, containing the types and placement heights/depths of the instruments.

The Southern Khentei Taiga (SKT) forest site is located in a Siberian larch forest on a southwest-facing gently sloping hill with a maximum slope of about 5° (Li et al., 2005b). The soil at the site is spodosol (seasonal cryosol) with coarse texture. Its total carbon content at the top 40 cm soil layer is $2.21 \pm 0.50\%$ on average after removal of roots by sieving. The understory was dense and formed a distinct layer of grasses and scattered shrubs (Li et al., 2005b). The temperate mixed forest site of Changbai mountain (CHB) is located in Northeastern China (Guan et al., 2006; Zhang et al., 2016). Elevational permafrost may occur in the upper part and on the top of the Changbai mountain (Wei et al., 2011). The Daxing'anling Forest Ecosystem Research Station (DXF) lies in a continuous permafrost region within northeastern China (Wei et al., 2011). The larch forest and frozen soil maintain the cold and wet environmental conditions of cold temperate coniferous forests (Tian et al., 2018). The annual frozen period is over 210 days and the snow cover exists from late September to early May (Chen and Li, 2008). The Kherlenbayan Ulaan (KBU) steppe site is located in northeastern Mongolia. It is fairly open and flat with terrain slopes less than 0.5° in all directions (Li et al., 2005a). The soil is classified as chestnut soil

Table 1 Description and location of sites. The detailed information about these sites is shown in the supplementary materials (Table S1).

Site ID	Site names	Period	Latitude, Longitude	Elevation (m asl)	Veg. types ^b	Frozen ground type ^a	Soil texture	T _{air} ^c (°C)	Precip ^b (mm)	D _{snow} ^b (cm)	H _{canopy} ^b (m)	Max LAI	CI ^b	Reference
SKT	Southern Khentei	2003–2006	48.35°N, 108.65°E	1630	DNF	Discontinuous permafrost	Sandy loam	-2.7	296	N/A	20	2.2	0.80 ^e	(Frazer et al., 2001; Li et al., 2005b)
CHB	Taiga Changbai	2003–2005	42.40°N, 128.10°E	738	MF	Seasonally frozen ground	Loam	3.6	713	10	25	5.8	0.69	(Gian et al., 2006)
DXF	Daxing'anling Forest	2013–2014	50.96°N, 121.51°E	832	DNF	Continuous permafrost	Loam	-5.4	500	13	27.5	2.41 ^d	0.56	(Wei et al., 2011; X. Zhang et al., 2018)
KBU	Kherlenbayan Ulaan	2004–2005	47.21°N, 108.74°E	1235	Grassland	Isolated permafrost	Clay loam	1.2	196	N/A	0.12	0.6	0.80 ^e	(Li et al., 2008, 2006, 2005a)
CNG	Changling	2007–2010	44.59°N, 123.51°E	171	Grassland	Seasonally frozen ground	Silt loam	5	400	2	0.75	3.0	0.82	(Dong et al., 2011)

^a The frozen ground type is extracted from the Circum-Arctic Map of Permafrost (Brown et al., 2002).

^b Veg. type: vegetation types; DNF: deciduous needleleaf forest; MF: mixed forest; T_{air}: mean annual air temperature; Precip: mean annual precipitation; D_{snow}: annual max snow depth (Che et al., 2008); H_{canopy}: mean canopy height; CI: leaf clumping index.

^c Data were extracted from a global MODIS-derived clumping index map at 500 m spatial resolution (He et al., 2012).

^d This LAI data is retrieved from the GLOMAP-V2 datasets at 8 km spatial resolution (Liu et al., 2012).

(Kastanozem), and is well-drained with low moisture-holding capacity (Li et al., 2008). Its bulk density, overall porosity, and hydraulic conductivity in the top 30 cm layer are 1.45 g cm⁻³, 45%, and 0.01~0.08 mm s⁻¹, respectively (Li et al., 2006). The Changling temperate meadow steppe station (CNG) is situated in the southern Songnen Plain. There is 1.5% soil organic matter in the top soil layer (Dong et al., 2011). The frost-free period was about 130~165 days and the growing season was limited to late April to September.

The vertical profile of soil organic carbon density and bulk density were derived from the SoilGrids dataset that covers the top 2 m of soil column with seven layers (0, 5, 15, 30, 60, 100, and 200 cm) (Hengl et al., 2017). The SoilGrids dataset with 250 m spatial resolution is interpolated to the five layers of soil column in the BEPS model using the linear interpolation method.

2.2. The description of BEPS model

The BEPS model, a process-based diagnostic model, was initially developed for Canadian boreal ecosystems (Liu et al., 1997), and has been adapted for other ecosystems over the globe. It is commonly used in stimulating photosynthesis, vegetation productivity, and soil biogeochemical processes at hourly time steps (Chen et al., 2016; J. M. Chen et al., 2019; S. Zhang et al., 2018). BEPS includes a “two-leaf” canopy stratification scheme that treats vegetation canopy as two groups of leaves, sunlit and shaded ones (B. Chen et al., 2019). The soil profile is divided into five layers and the thickness of soil layers increases exponentially from the top layer to the deepest layer (equals to 0.05, 0.1, 0.2, 0.4, and 1.25 m, respectively). Each soil layer is considered as a mixture of mineral soil, organic matter and water (Fig. 2). The BEPS model is driven by vegetation parameters, including leaf area index, clumping index, and land cover type, as well as meteorological and soil data.

BEPS includes modules to calculate the thermal dynamics of soil profile, which are determined using a one-dimensional (vertical direction) heat diffusion equation (Chen et al., 2007):

$$C_{s,l} \frac{\partial T_{s,l}}{\partial t} = \frac{\partial}{\partial z} \left(\lambda_{t,l} \frac{\partial T_{s,l}}{\partial z} \right) + S_{s,l}, \quad (1)$$

where $C_{s,l}$ (J m⁻³ K⁻¹) is the volumetric heat capacity of soil layer l ; $T_{s,l}$ (°C) is the soil temperature at depth z and time t . $S_{s,l}$ (W m⁻³) is the source (or sink) term for freezing or thawing of moisture occurred at soil layer l . $\lambda_{t,l}$ (W m⁻¹ K⁻¹) is the soil thermal conductivity, which is determined as a function of soil texture and soil moisture content (Kumar and Kaleita, 2003):

$$\lambda_{t,l} = [\lambda_{s,l}^{(1-\theta_{sat,l})} \lambda_{liq}^{\theta_{w,l}(1-f_{ice,l})} \lambda_{ice}^{\theta_{w,fice,l}} - 0.15] \frac{\theta_{w,l}}{\theta_{sat,l}} + 0.15 \quad (2)$$

where $\lambda_{s,l}$, λ_{liq} and λ_{ice} are the thermal conductivity of the constituents, including soil solids (decided by soil texture), liquid water (0.61 W m⁻¹ K⁻¹), and ice (2.2 W m⁻¹ K⁻¹). $\theta_{sat,l}$ is the saturated soil moisture. The soil organic matter (SOM) was not considered in the calculation of λ . Calculation of other properties and heat transfer processes of soil profile are shown in Appendix A.

2.3. Model improvements

2.3.1. Snowpack density

Snowpack controls the thermal transmission through the atmosphere-soil interface during winter and early spring (Wu et al., 2016). In the original BEPS model, the snow density (ρ_{snow}) is calculated simply as:

$$\rho_{snow} = 67.9 + 51.3e^{\frac{T_a}{6}} \quad (3)$$

where T_a is air temperature. The effects of canopy and wind speed on ρ_{snow} was not considered.

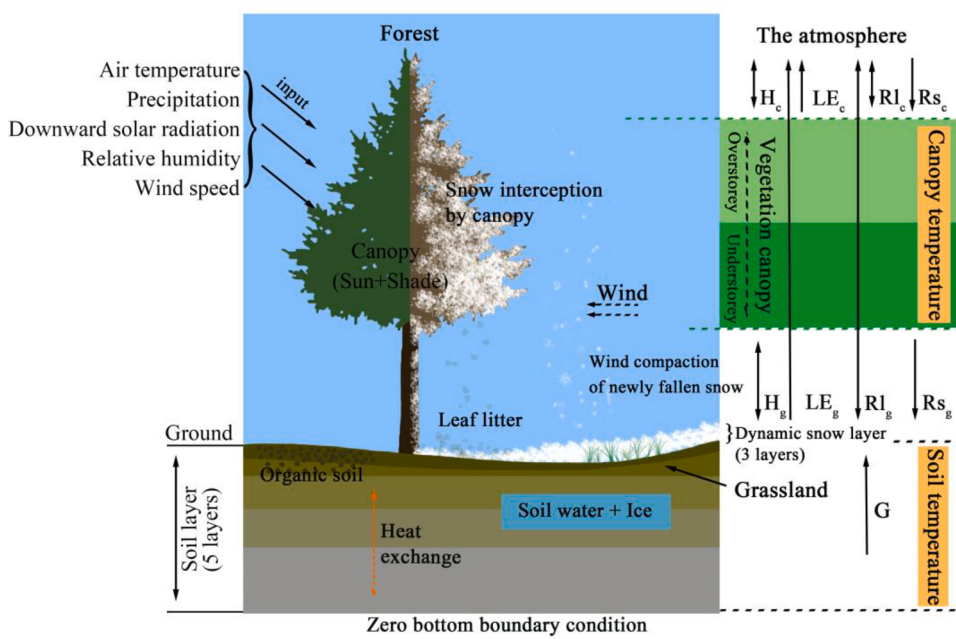


Fig. 2. Conceptualized diagram of the thermal transfer module in the BEPS model, focusing on the underlying mechanisms controlling ground temperature and soil freeze-thaw processes in cold regions. H , LE , RL , Rs , and G are the sensible heat flux, latent heat flux, longwave radiation, shortwave radiation, and net energy flux from soil column, respectively; the subscripts c and g represent atmosphere-canopy and canopy-soil interfaces, respectively. The temperature includes the air temperature (input), the sunlit and shaded canopy temperature for both overstorey and understory, the snow temperature (if snow is present), the ground temperature, and the soil temperature of different layers.

In the improved BEPS model, the snow accumulation is correlated closely with the canopy characteristics. For the windy grassland sites, ρ_{snow} is calculated as (Helfricht et al., 2018):

$$\rho_{\text{snow}} = \begin{cases} 500(1 - 0.951e^{-1.4(5-T_a)^{-1.15}} - 0.008u^{1.7}), & -13^{\circ}\text{C} < T_a < 2.5^{\circ}\text{C} \\ 500(1 - 0.904e^{-0.008u^{1.7}}), & T_a \leq -13^{\circ}\text{C} \end{cases} \quad (4)$$

where T_a ($^{\circ}\text{C}$) is air temperature, u is the wind speed in m/s.

2.3.2. Puddled water

In the case that the surface water supply (e.g., rainfall, snowmelt, or irrigation) exceeds the actual infiltration rate from the surface into the soil, the BEPS model assumes that a puddle occurs (Chen et al., 2007). The puddled water has large specific heat and it can buffer the variation of ground temperature. The hydro-dynamics of surface water supply and infiltration were implemented in the original BEPS model (Chen et al., 2007). However, the influences of surface water on surface thermal transmission have not been considered yet.

In the improved BEPS model, the thermal regime of the puddle is distinguished from that of underneath soil. The puddle is modeled as part of the profile for heat conduction within the SNOWPACK module. Puddle and snowpack (or surface ice) can be converted into each other at freezing point (0°C). The amount of meltwater and freezing water is estimated based on the available energy. Similarly to the calculation of snowpack temperature (Chen et al., 2007), the temperature of puddled water is first calculated using Eq. (1), without considering the thawing/freezing effects and this is apparent temperature (T'_s). If $T'_s < 0^{\circ}\text{C}$, energy would be released from water freezing. T_s is then reset to 0°C .

2.3.3. Soil organic matter

In the original BEPS model, soil organic matter was not considered in the calculation of some soil thermal-hydraulic parameters such as soil thermal conductivity, the saturated soil water potential, the Clapp and Hornberger empirical parameter and the saturated hydraulic conductivity. The SOM usually has high heat capacity and low heat conductivity due to its high porosity with a majority of pores filled with water and air. Neglecting SOM in the calculation of soil thermal-hydraulic parameters would cause large uncertainties in simulating soil thermal dynamics.

In the improved BEPS model, we replaced the default parameterization of soil thermal conductivity (λ_l) with that of Tian et al. (2016) as:

$$\lambda_l = \frac{\lambda_{\text{liq},l}\theta_{\text{liq},l} + w_{\text{ice},l}\lambda_{\text{ice},l}\theta_{\text{ice},l} + w_{a,l}\lambda_{a,l}\theta_{a,l} + w_{s,l}\lambda_{s,l}\theta_{s,l} + w_{\text{soc},l}\lambda_{\text{soc},l}\theta_{\text{soc},l}}{\theta_{\text{liq},l} + w_{\text{ice},l}\theta_{\text{ice},l} + w_{a,l}\theta_{a,l} + w_{s,l}\theta_{s,l} + w_{\text{soc},l}\theta_{\text{soc},l}} \quad (5)$$

where the subscript a denotes the air component, subscript soc denotes the soil organic carbon, θ is the volumetric fraction, and w is the “weighting” factor (unitless) (Appendix B1).

The calculations of other soil thermal-hydraulic parameters were also improved to incorporate the effects of SOM and they are expressed as (Lawrence and Slater, 2008):

$$\alpha_l = (1 - f_{\text{soc},l})\alpha_{\text{min},l} + f_{\text{soc},l}\alpha_{\text{soc}} \quad (6)$$

where the subscripts soc and min represent the soil organic carbon and mineral material; $f_{\text{soc},l}$ is the volume fraction of soil organic carbon in soil layer l ; α is any hydrologic or thermal parameter. In the improved BEPS model, the thermal conductivity of SOM (λ_{soc}) is set as $0.25 \text{ W m}^{-1} \text{ K}^{-1}$ (Farouki, 1981), the saturated soil water potential of SOM ($\Psi_{\text{sat}, \text{soc}}$) is set as -10.3 mm , the Clapp and Hornberger empirical parameter of SOM (b) is set as 2.7 , and the saturated hydraulic conductivity of SOM ($k_{\text{sat}, \text{soc}}$) is set as $0.10 \text{ m s}^{-1} \times 10^{-3}$ (Letts et al., 2000).

2.3.4. Super-cooled soil water

The original BEPS model did not consider the super-cooled soil water which can exist in frozen soils through the capillary and absorptive forces exerted by soil particles (Melton et al., 2019). This liquid water content changes drastically near 0°C and decreases with decreasing temperature. Its amount has important implications for the simulation of thermal dynamics in frozen soils (Hu et al., 2020b; Zhang et al., 2008).

In the improved BEPS model, we set the upper limit of the liquid water content for subfreezing temperature as (Niu and Yang, 2006):

$$\theta_{\text{liq},\text{max}} = \theta_{\text{sat}} \left[\frac{10^3 L_f (T - T_{\text{frz}})}{g T \psi_{\text{sat}}} \right]^{-\frac{1}{b}} \quad (7)$$

where θ_{sat} is the porosity of soil; L_f is the latent heat of fusion (J kg^{-1}); T and T_{frz} are soil temperature and freezing point ($^{\circ}\text{C}$) ($T_{\text{frz}} = 0^{\circ}\text{C}$), respectively (Fuchs et al., 1978); g is the gravitational acceleration (m s^{-2}); ψ_{sat} is the saturated soil matric potential depending on the soil

Table 2
Intercepts (a), slopes (b), coefficients of determination (R^2), root mean square of errors (RMSE) from regressions of hourly soil temperature simulated by the original and improved BEPS model vs hourly soil temperature measured at the five studied sites. The scatter plots between simulations and observations at each site are shown in the supplementary materials (Figs. S2 and S3).

Site ID	Periods	Veg. types ^a	a Original	a Improved	b Original	b Improved	R^2	RMSE (°C)	n
SKT	2003–2006	DNF	-2.53	-0.99	1.41	1.09	0.94	5.44	Improved
CHB	2003–2005	MF	-5.06	0.31	1.43	1.02	0.90	6.01	Original
DXF	2013–2014	DNF	-1.59	0.95	1.09	0.93	0.98	1.79	Improved
KBU	2004–2005	Grassland	-2.49	-0.86	0.92	0.90	0.94	2.33	Original
CNG	2007–2010	Grassland	-2.65	0.24	1.19	1.05	0.96	3.31	Improved

^a Veg. types: vegetation types. DNF: deciduous needleleaf forest; MF: mixed forest.

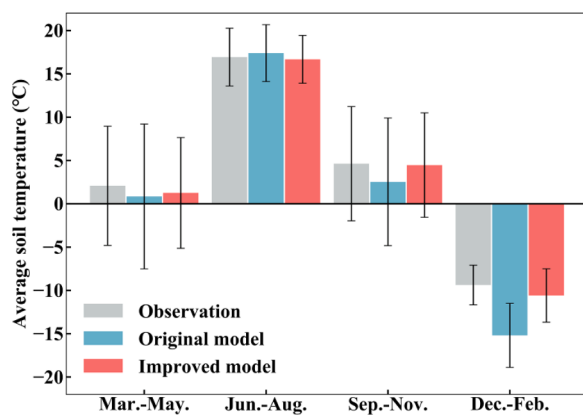


Fig. 3. Ensemble averages of seasonal variations in soil temperature of the five studied sites from observation, the original and improved BEPS model. The error bars represent the standard deviation. The detailed values shown in this figure are displayed in the supplementary materials (Table S2).

texture (mm); and b is the Clapp and Hornberger empirical parameter (Clapp and Hornberger, 1978). This equation calculates the maximum liquid water content at a soil temperature below the freezing point (Appendix B2).

2.4. Estimation of soil freeze-thaw parameters

The periods of soil thawing and freezing are determined by soil temperature. A soil FT cycle occurs when the daily maximum soil temperature exceeds 0 °C and the daily minimum soil temperature is below 0 °C, which means the soil thaws during the day and is frozen during the night. The duration of the diurnal soil FT cycles is calculated as the number of days with the diurnal soil FT cycle. The amplitude of the diurnal soil FT cycles is calculated using the difference between the daily maximum and minimum soil temperature when the diurnal soil FT cycle occurs. Thaw/freeze day is defined as the onset date of soil thawing/freezing.

3. Results

3.1. Simulation of soil temperature

The hourly soil temperature simulated by the original and improved BEPS model were compared with measured data to evaluate the performance of the original and improved BEPS model in simulating soil temperature at the studied sites (Supplementary materials, Fig. S1). The regression statistics are summarized in Table 2. The original and improved BEPS models are both able to explain >90% of the variance in soil temperature. The root mean square error (RMSE) of soil temperature simulated by the original BEPS model ranges from 2.33 to 6.01 °C and that simulated by the improved BEPS model ranges from 1.79 to 3.31 °C (Table 2). The improved BEPS model shows smaller RMSEs, higher R^2 and slopes closer to one, performed better than the original BEPS model in simulating soil temperature at the studied sites.

Simulated seasonal soil temperature from both the original and improved BEPS model were also compared with the observed soil temperature for all the studied sites (Fig. 3). In general, both the original and improved BEPS models were able to capture the seasonal variations in soil temperature for the studied sites and the improved BEPS model performed better than the original one in simulating ensemble mean soil temperate in all four seasons (Fig. 3).

In spring (Mar. to May), the observed ensemble mean soil temperature was 1.94 ± 6.84 °C while the simulated soil temperature from the original and the improved BEPS model were 0.57 ± 8.26 °C and 1.19 ± 6.30 °C, respectively (Fig. 3). On average, the improved BEPS model

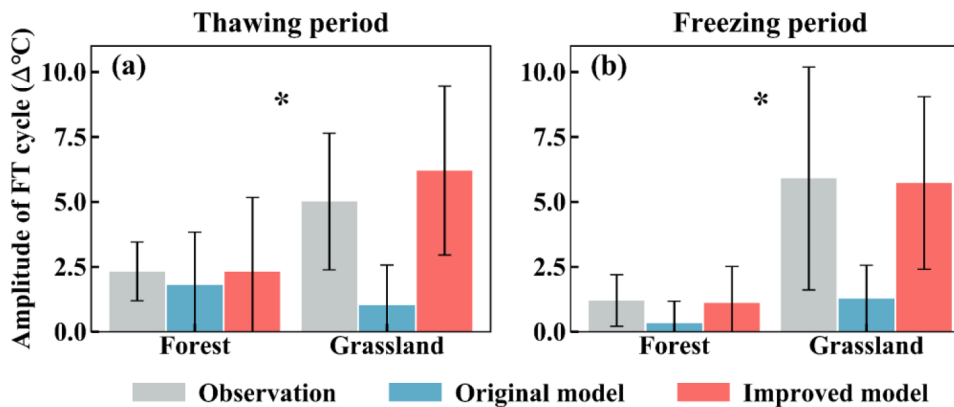


Fig. 4. The mean amplitudes of diurnal soil FT cycles of the studied forest and grassland sites from observation, the original and improved BEPS model for thawing and freezing periods, respectively. The error bars represent the standard deviations. Using double-tailed t-tests, the differences in the amplitudes of FT cycles between forest and grassland for both thawing and freezing periods are all statistically significant ($p < 0.1$) based on the observation and the simulated results of the improved BEPS model. One star represents $p < 0.1$. The amplitudes of diurnal soil FT cycles of each site are shown in the supplementary materials (Fig. S4).

underestimated the observed soil temperature by 38.7% in spring. This negative bias is much smaller than that of the original BEPS model which is as large as 70.6%.

In summer, the observed ensemble mean soil temperature was 16.97 ± 3.36 °C while the simulated soil temperature from the original and the improved BEPS model were 17.37 ± 3.26 °C and 16.67 ± 2.74 °C, respectively (Fig. 3). On average, the improved BEPS model underestimated the observed soil temperature by 1.8% while the original BEPS model overestimated observed soil temperature by 2.4% in summer.

In autumn, the observed ensemble mean soil temperature was 4.59 ± 6.70 °C while the simulated soil temperature from the original and the improved BEPS model were 2.49 ± 7.50 °C and 4.44 ± 6.08 °C, respectively (Fig. 3). On average, the improved BEPS model underestimated the observed soil temperature by 3.4% in autumn. This negative bias is much smaller than that of the original BEPS model which is as large as 45.8%.

In winter, the observed ensemble mean soil temperature was -9.41 ± 2.39 °C while the simulated soil temperature from the original and the improved BEPS model were -15.33 ± 3.87 °C and -10.47 ± 3.36 °C, respectively (Fig. 3). On average, the improved BEPS model underestimated the observed soil temperature by 11.3% in winter. This negative bias is much smaller than that of the original BEPS model which is as large as 62.9%.

3.2. Simulation of diurnal soil FT cycles of different vegetation types

Mean amplitudes of diurnal soil FT cycles simulated by the original and improved BEPS model are compared with those from the observations at the studied forest and grassland sites for thawing and freezing periods, respectively (Fig. 4). The observed mean amplitudes of soil diurnal FT cycles during the thawing period are 2.32 ± 1.06 °C at forest

sites and 5.01 ± 2.35 °C at grassland sites (Fig. 4a). The simulated mean amplitudes of soil diurnal FT cycles from the original and improved BEPS model during the thawing period are 1.80 ± 1.91 °C and 2.31 ± 2.68 °C, respectively, at forest sites and they are 1.03 ± 1.38 °C and 6.21 ± 2.91 °C, respectively, at grassland sites (Fig. 4a). The results from the improved BEPS model are closer to the observations compared to those from the original BEPS model.

During freezing period, the observed mean amplitudes of diurnal soil FT cycles are 1.20 ± 0.92 °C at forest sites and 5.91 ± 3.84 °C at grassland sites (Fig. 4b). The simulated mean amplitudes of diurnal soil FT cycles from original and improved BEPS model during the freezing period are 0.32 ± 0.79 °C and 1.10 ± 1.30 °C, respectively, at forest sites and they are 1.28 ± 1.15 °C and 5.73 ± 2.97 °C, respectively, at grassland sites (Fig. 4b). The results from the improved BEPS model are closer to the observations compared to those from the original BEPS model.

The mean amplitudes of diurnal soil FT cycles are larger at grassland sites than forest sites for both thawing and freezing periods (Fig. 4). Through the conventional double-tailed t-tests, the differences in amplitudes of FT cycles between forest and grassland sites for both thawing and freezing periods are all statistically significant at $p < 0.1$, meaning that the vegetation effect for either thawing period or freezing period is highly significant.

Mean durations of diurnal soil FT cycles simulated by the original and improved BEPS model are also compared with those from the observations at the studied forest and grassland sites for thawing and freezing periods, respectively (Fig. 5). The observed mean durations of diurnal soil FT cycles during the thawing period are 14 ± 5 days at forest sites and 11 ± 6 days at grassland sites (Fig. 5a). The simulated mean durations of diurnal soil FT cycles from the original and improved BEPS model during the thawing period are 2 ± 2 days and 9 ± 5 days, respectively, at forest sites and they are 1 ± 2 days and 8 ± 5 days,

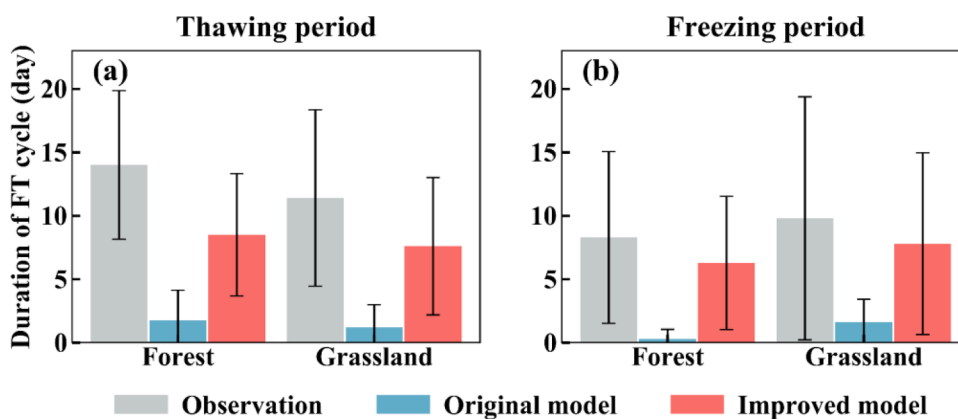


Fig. 5. The mean durations of diurnal soil FT cycles of the studied forest and grassland sites from observation, the original and improved BEPS model for thawing and freezing periods, respectively. The error bars represent the standard deviations. Using double-tailed t-tests, the differences in durations of FT cycles between forest and grassland for both thawing and freezing periods are not statistically significant ($p > 0.1$) based on the observation and the simulated results of the improved BEPS model. The durations of diurnal soil FT cycles of each site are shown in the supplementary materials (Fig. S5).

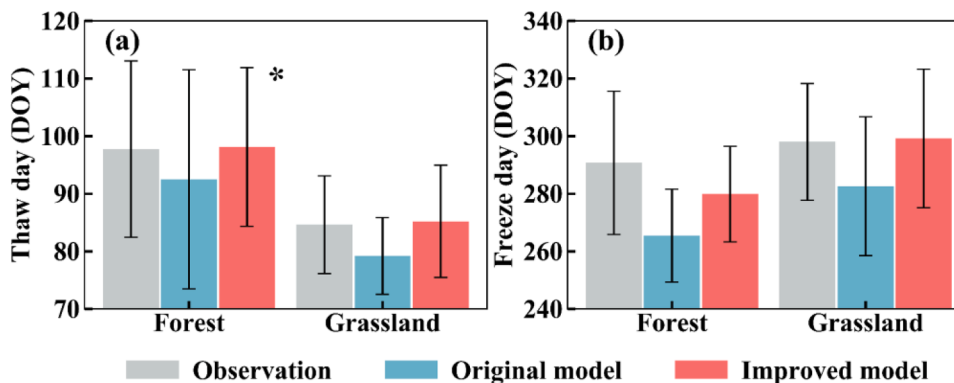


Fig. 6. The thaw day and freeze day of forest and grassland sites. The error bars represent the standard deviation. Using double-tailed t-tests, the difference of the thaw day between forest and grassland is statistically significant ($p < 0.1$) while the difference of the freeze day between forest and grassland is not statistically significant ($p > 0.1$) based on the observation and the simulated results of the improved BEPS model. One star represents $p < 0.1$ and no star represents $p > 0.1$. DOY means day of the year. The thaw day and freeze day of each site are shown in the supplementary materials (Fig. S6).

respectively, at grassland sites (Fig. 5a). The results from the improved BEPS model are closer to the observations compared to those from the original BEPS model.

During the freezing period, the observed mean durations of diurnal soil FT cycles are 8 ± 6 days at forest sites and 10 ± 9 days at grassland sites (Fig. 5b). The simulated mean durations of diurnal soil FT cycles from the original and improved BEPS model during the freezing period are 1 ± 1 days and 6 ± 5 days, respectively, at forest sites and they are 2 ± 2 days and 8 ± 6 days, respectively, at grassland sites (Fig. 5b). The results from the improved BEPS model are closer to the observations compared to those from the original BEPS model.

3.3. Simulation of seasonal soil FT timing for different vegetation types

Mean thaw days simulated by the original and improved BEPS model are compared with those from the observations at the studied forest and grassland sites, respectively (Fig. 6a). The observed mean thaw days are DOY 98 ± 14 at forest sites and DOY 85 ± 8 at grassland sites (Fig. 6a). The simulated mean thaw day from the original and improved BEPS model are DOY 93 ± 18 and DOY 98 ± 13 , respectively, at forest sites and they are DOY 79 ± 6 and DOY 85 ± 9 , respectively, at grassland sites (Fig. 6a). The results from the improved BEPS model are closer to the observations compared to those from the original BEPS model. The soil of forest sites thawed later than grassland sites. Through the conventional double-tailed t-tests, the differences of thaw day between forest and grassland sites are statistically significant at $p < 0.1$, based on the observation and the simulated results of the improved BEPS model (Fig. 6a).

Mean freeze days simulated by the original and improved BEPS model are also compared with those from the observations at the studied forest and grassland sites, respectively (Fig. 6b). The observed mean freeze days are DOY 291 ± 23 at forest sites and DOY 298 ± 18 at grassland sites (Fig. 6b). The simulated mean freeze days from the original and improved BEPS model are DOY 265 ± 15 and DOY 282 ± 19 , respectively, at forest sites and they are DOY 283 ± 22 and DOY 299 ± 21 , respectively, at grassland sites (Fig. 6b). The results from the improved BEPS model are closer to the observations compared to those from the original BEPS model. Through the conventional double-tailed t-tests, the differences of freeze days between forest and grassland sites are not statistically significant at $p > 0.1$, based on the observation and the simulated results of the improved BEPS model (Fig. 6b).

4. Discussion

4.1. The impacts of different improvement schemes on the simulations of soil temperature

The Gaussian kernel density estimation (KDE) of the differences between the simulated soil temperatures from the experimental model runs and the observations of the five studied sites was conducted to

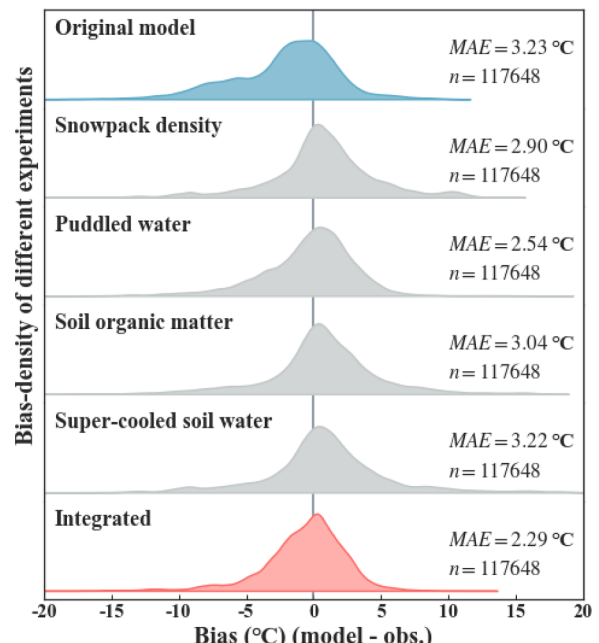


Fig. 7. The Gaussian kernel density estimation (KDE) of the differences between the hourly soil temperatures from the experimental model runs and those measurements of the five studied sites. The more concentrated the data is on the center zero line, the higher the accuracy. The gray KDE plots represent the distributions of the simulation biases of each improvement scheme. The red KDE plot represents the distribution of simulation biases of the improved BEPS model, which integrated all improvement schemes. MAE represents mean absolute error.

compare the contribution of the four modifications of BEPS model in simulating soil temperature. Considering the impacts of canopy and wind speed on the snowpack density reduces the MAE of simulated soil temperature from 3.23 to 2.90°C (Fig. 7). The incorporation of puddled water into the simulation of soil thermal dynamics reduces the MAE of simulated soil temperature from 3.23 to 2.54°C (Fig. 7). The incorporation of soil organic matter into the calculations of soil thermal-hydraulic parameters reduces the MAE of simulated soil temperature from 3.23 to 3.04°C (Fig. 7). The inclusion of unfrozen water in frozen soils did not change MAE of simulated soil temperature significantly (Fig. 7). Totally, the integrated improvements to the BEPS model reduce the MAE of simulated soil temperature from 3.23 to 2.29°C (Fig. 7).

The simulations of soil temperature from the improved BEPS model perform much better than those of the original BEPS model due to more careful treatments of the impacts of a thermal “buffer zone” (i.e. snowpack, puddled water and SOM) on subsurface heat transfer. Snow is an insulator and is a leading factor in preventing the ground from heat

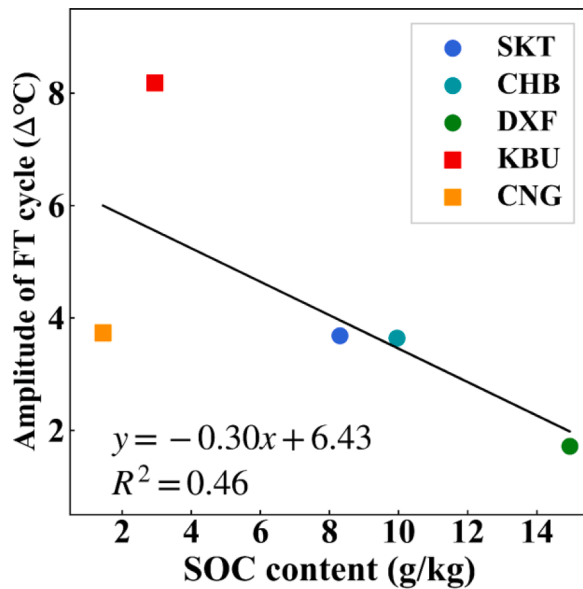


Fig. 8. The mean soil organic carbon (SOC) content in the surface soil layer (2.5 cm) versus the mean amplitudes of diurnal soil FT cycles during thawing periods at the studied sites. Blue and green circles represent forest sites. Red and orange squares represent grassland sites. The data of SOC content are derived from site observation and SoilGrids dataset and are used as the input data to the BEPS model. The amplitudes of FT cycles are simulated by the improved BEPS model.

loss in winter, especially at the high latitudes where stable snow cover lasts from a few weeks to several months (Zhang, 2005). As an aquitard, the frozen soil layer drastically weakens hydraulic connectivity and downward water infiltration and benefits the existence of puddled water

(Jin et al., 2020). The puddled water layers act as a buffer that modulates the heat exchange between the overlying air and the underlying soil layer. SOM would also modulate the transfer of heat between soil and atmosphere, typically leading to a smaller daily difference in soil temperature (Lawrence and Slater, 2008). Thus, it is essential to incorporate a realistic buffer zone between the atmospheric forcing and soil thermal processes (Ju et al., 2006; Kim et al., 2016; Tao et al., 2017).

4.2. Vegetation types affected diurnal soil FT cycles and seasonal soil ft timing

Different vegetation types have distinct community structures and consequently differ in litter cover, snow accumulation patterns, and canopy interception of solar radiation (Guo et al., 2018; Wang et al., 2002). Plant litter is a major source of near-surface SOM, and the accumulation of litter was affected by plant species (Novara et al., 2015). Compared to grassland, the forest usually has more aboveground biomass, thicker litter layer and more SOM (Supplementary materials, Fig. S7). Thus, litter insulation is higher in forest sites, producing a lower amplitude of diurnal soil FT cycles compared to grassland sites (Fig. 8).

It has been recognized that snow accumulation differs substantially between forested and grassland because of the difference in canopy interception of snow, snow sublimation and wind redistribution (Chang et al., 2015; Foster et al., 2019). The mean snow depth is positively correlated with the thaw day (Fig. 9b) because the depth-dependent snowpack insulation could regulate the thermal transmission between the atmosphere and the soil and consequently slow down soil thawing. Also, the SOC content is positively correlated with the thaw day (Fig. 9d) because SOM also buffers soil thermal transmission and more soil surface SOC would slow down soil thawing during the thawing period. Forest sites have thicker snow depth and more soil surface SOC than grassland sites and these are the reasons why the thaw days of forest sites are later than those of grassland sites (Fig. 9).

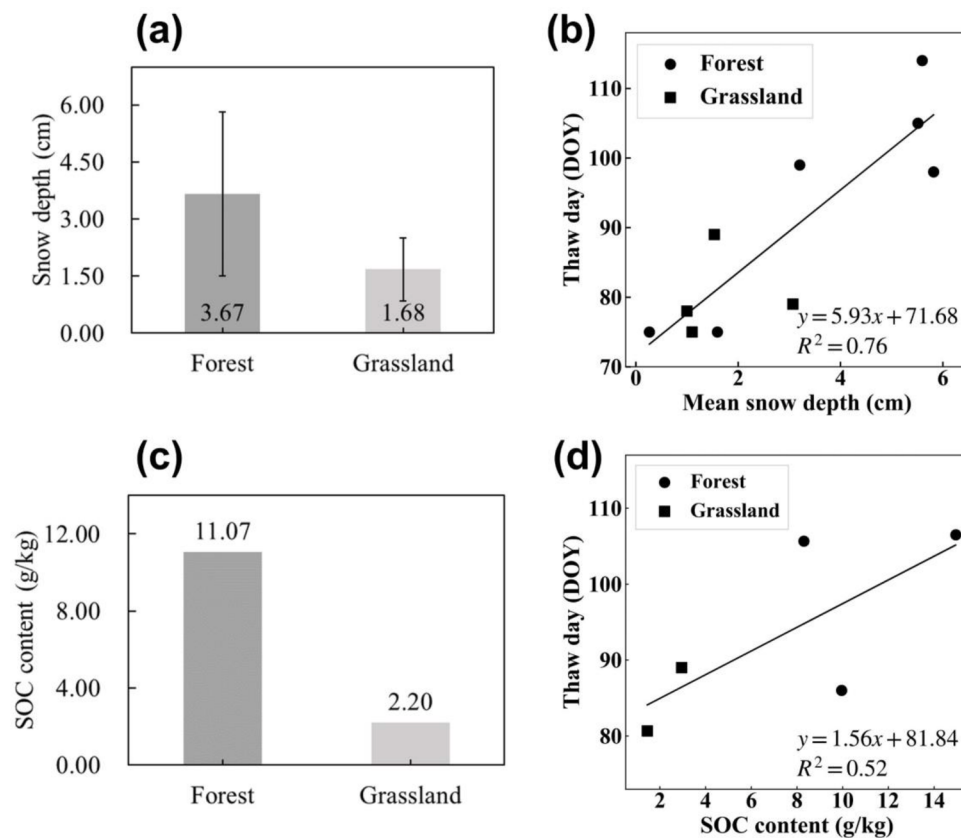


Fig. 9. The ensemble averages of daily snow depth during winter (a) and the relationship of mean snow depth and the thaw day (b) for the forest and grassland sites. The ensemble averages of SOC content in the surface soil layer (2.5 cm) (c) and the relationship of SOC content in the surface soil layer (2.5 cm) and the thaw day (d) for the forest and grassland sites. The snow depth and thaw day are simulated by the improved BEPS model. The data of SOC content are derived from site observation and SoilGrids dataset and are used as the input data to the BEPS model.

5. Conclusions

In this study, the BEPS model has been improved through more careful treatments of the impacts of thermal “buffer zone” (i.e. snowpack, puddled water and SOM) on subsurface heat transfer. The different patterns of soil surface FT processes between forest and grassland and the regulation of vegetation to soil FT processes were analyzed based on the measured soil temperature data and those simulated by the BEPS model. The major conclusions are drawn as follows:

- (1) Compared to the original BEPS model, the improved BEPS model has smaller RMSEs, higher R^2 and slopes closer to one, and performs better in simulating soil temperate in all four seasons.
- (2) The simulated diurnal soil FT cycles and seasonal soil FT timing from the improved BEPS model are closer to the observations compared to those from the original BEPS model.
- (3) Forest sites have smaller amplitudes of diurnal soil FT cycles and delayed timing of soil thaw compared to grassland sites.

CRediT

Zhenhai Liu: Conceptualization, Software, Writing - Original draft preparation.

Bin Chen: Conceptualization, Methodology, Writing - Review and Editing.

Shaoqiang Wang: Writing - Review and Editing, Supervision, Project administration.

Qinyi Wang: Validation, Data Curation.

Jinghua Chen: Software.

Weibo Shi: Software.

Xiaobo Wang: Software.

Yuanyuan Liu: Visualization.

Yongkai Tu: Visualization.

Mei Huang: Supervision.

Junbang Wang: Supervision.

Zhaosheng Wang: Supervision.

Hui Li: Data Curation.

Tongtong Zhu: Data Curation.

Declaration of Competing Interest

The authors declare that they have no known competing financial interests or personal relationships that could have appeared to influence the work reported in this paper.

Acknowledgments

The authors sincerely appreciate Prof. Jingming Chen for sharing the codes of the BEPS model. This study used eddy covariance data acquired and shared by ChinaFLUX, AsiaFlux and FLUXNET. The GLOMAP-V2 LAI datasets and SoilGrids dataset are provided by Yang Liu and Tomislav Hengl. We greatly offer our profound appreciation to all the providers of the freely available data. This research was supported by the Science and Technology Strategic Pilot of the Chinese Academy of Sciences (XDA20030203).

Supplementary materials

Supplementary material associated with this article can be found, in the online version, at [doi:10.1016/j.ecolmodel.2021.109663](https://doi.org/10.1016/j.ecolmodel.2021.109663).

Appendix A: Thermal dynamics of the soil profile in the original BEPS model

The soil volumetric heat capacity $C_{s,l}$ is equal to the sum of the specific heat capacities of the soil constituents (water, ice, soil minerals, and organic matter) multiplied by their respective volumetric fraction.

$$C_{s,l} = \frac{2.0 \times 10^3 \rho_{s,l}}{2.65} + (c_w(1-f_{ice,l}) + c_{ice}f_{ice,l})\theta_{w,l} + c_{s,soc}f_{soc,l} \quad (A1)$$

where $\rho_{s,l}$ (g cm^{-3}) is the soil bulk density of layer l ; c_w ($4.2 \times 10^3 \text{ J kg}^{-1} \text{ K}^{-1}$), c_{ice} ($2.09 \times 10^3 \text{ J kg}^{-1} \text{ K}^{-1}$), $c_{s,soc}$ ($2.5 \times 10^3 \text{ J kg}^{-1} \text{ K}^{-1}$) are the specific heat of water, ice, and soil organic matter, respectively; $\theta_{w,l}$ is the soil moisture in the l th soil layer; $f_{ice,l}$ and $f_{soc,l}$ are the volume fractions of ice and organic matter in soil layer l , respectively; 2.65 g cm^{-3} is the typical soil particle density of mineral soils; $2.0 \times 10^3 \text{ J kg}^{-1} \text{ K}^{-1}$ is the specific heat of mineral soils.

The net energy flux at the ground surface under canopy and snow (G_0) is assumed to be transmitted into soil layers as the boundary condition:

$$0 = G_0 + R_{ng} + H_g + \lambda E_g \quad (A2)$$

$$\frac{C_{s,l}\delta T_{s,l}}{\delta t} = \frac{G_{l-1,l} - G_{l,l+1}}{z_l + S_{s,l}} \quad (l=1, 2, 3, \dots, N-1) \quad (A3)$$

$$G_{l-1,l} = G_{0,1} = G_0 \quad (l=1) \quad (A4)$$

$$G_{l-1,l} = \frac{(0.5k_{l,l-1} + 0.5k_{l,l})(T_{s,l-1} - T_{s,l})}{0.5z_{l-1} + 0.5z_l} \quad (l=2, 3, 4, \dots, N) \quad (A5)$$

where R_{ng} (W m^{-2}) is the net absorbed radiation by a canopy; H_g (W m^{-2}) is the sensible heat flux from the ground to the canopy and through it; λ (J kg^{-1}) is the latent heat of vaporization; E_g ($\text{kg m}^{-2} \text{ s}^{-1}$) is the evaporation from the ground surface; $G_{l-1,l}$ (W m^{-2}) is the conductive heat fluxes between soil layers $l-1$ and l .

The snowpack is modeled as a part of the profile for heat conduction below the reference plane of surface temperature. The same equation for heat dynamics in the soil profile is used in the snowpack thermal module. The amount of snow is the balance of snowfall and snowmelt, which is estimated based on the available energy. The thickness of the snowpack is updated every time step based on the amount of snow (water equivalent) and its density profile. When the thickness of the snowpack covering the ground is less than 2 cm, the snowpack and ground surface is considered as one layer. When the thickness is more than 2 cm but less than 5 cm, the snowpack, as an independent layer on the ground, is proportionally distributed with bare

ground. When the thickness is greater than 5 cm, the snowpack is regarded as three layers (0~2 cm, 2~5 cm, and > 5 cm).

Appendix B: Description of improved parameterizations

B1. Soil organic matter

The parameterization of soil thermal conductivity is based upon the “weighting” factor w of different components to calculate the λ . The w is given as (Tian et al., 2016):

$$w_{s,l} = \frac{1}{3} \left[\frac{2}{1 + 0.125 \left(\frac{\lambda_{s,l}}{\lambda_{liq,l}} - 1 \right)} + \frac{1}{1 + 0.75 \left(\frac{\lambda_{s,l}}{\lambda_{liq,l}} - 1 \right)} \right] \quad (\text{B1})$$

$$w_{a,l} = \frac{1}{3} \left[\frac{2}{1 + g_a \left(\frac{\lambda_a}{\lambda_{liq,l}} - 1 \right)} + \frac{1}{1 + (1 - 2g_a) \left(\frac{\lambda_a}{\lambda_{liq,l}} - 1 \right)} \right], \quad (\text{B2})$$

where g_a represents a unitless empirical air pore-shape factor:

$$g_a = 0.333 - \left(1 - \frac{\theta_{a,l}}{\theta_{sat,l}} \right) \quad (\text{B3})$$

The shape of ice crystal in soil pores develop similarly to those of air voids. Therefore, g for ice is given by the following equation:

$$g_{ice} = 0.333 - \left(1 - \frac{\theta_{ice,l}}{\theta_{sat,l}} \right) \quad (\text{B4})$$

The thermal conductivity of air $0.025 \text{ W m}^{-1} \text{ K}^{-1}$. The heat capacity ($C_{s,l}$) of a soil layer l is calculated through updated formula as (Lawrence and Slater, 2008):

$$C_{s,l} = c_{s,l}(1 - \theta_{sat,l}) + (c_w(1 - f_{ice}) + c_{ice}f_{ice})\theta_{l,w} + c_{air}(\theta_{sat,l} - \theta_{w,l}) \quad (\text{B5})$$

$$c_{s,l} = c_{s,min,l}(1 - f_{soc,l}) + c_{s,soc}f_{soc,l} \quad (\text{B6})$$

where c_{air} ($1.0 \times 10^3 \text{ J kg}^{-1} \text{ K}^{-1}$) is the specific heat of air in soil layers (de Vries, 1963); $c_{s,min,l}$ is the specific heat of mineral soil and is computed as the percent of sand and clay for soil layer l . The soil organic carbon fraction ($f_{soc,l}$) for a particular soil layer as $f_{soc,l} = \rho_{soc,l}/\rho_{soc,max}$. The $\rho_{soc,l}$ is the soil carbon density for soil layer l and $\rho_{soc,max}$ (130 kg m^{-3}) is the maximum soil carbon density (equivalent to a standard bulk density of peat) (Farouki, 1981). The specific heat capacity of soil layer l is the weighted sum of the specific heat of soil solid and water.

B2. Unfrozen water content in frozen soil

The upper limit of the liquid water content for subfreezing temperature is calculated by Eq. (7). Based on $\theta_{liq,max}$, the content of liquid water in frozen soils for the next time step ($N+1$) is calculated as follows:

$$\theta_{liq}^{N+1} = \min(\theta_{liq,max}, \theta^N) \quad (\text{B7})$$

where $\theta^N = \theta_{liq} + \theta_{ice}$ is the total volumetric soil moisture at time step N . θ_{ice} is the ice content. The θ_{ice} for the next time step is defined as:

$$\theta_{ice}^{N+1} = \min(\theta_{ice}^N + R_{fm}\Delta t, \theta^N) \quad (\text{B8})$$

where Δt is the time step; R_{fm} is the conservation of the partial volume of ice:

$$\frac{\partial \theta_{ice}}{\partial t} = R_{fm} \quad (\text{B9})$$

and R_{fm} is defined as:

$$R_{fm} = \frac{H_{fm}}{\rho_{ice} L_f \Delta z} \quad (\text{B10})$$

where ρ_{ice} (917 kg m^{-3}) is the density of ice. H_{fm} in the unit of W m^{-2} is assessed from the energy excess or deficit needed to change soil temperature to the freezing point (T_{frz}) and it is calculated as:

$$H_{fm} = C_s \Delta z \frac{T_{frz} - T^{N+1}}{\Delta t} \quad (\text{B11})$$

where T^{N+1} is the soil layer temperature resulting from all the other processes except for phase changes. The soil hydraulic conductivity, k (m s^{-1}), can be calculated via the Clapp and Hornberger (1978) equation as:

$$k = f_{ice} k_{sat} \left(\frac{\theta_{iq}}{\theta_{sat}} \right)^{2b+3} \quad (B12)$$

where k_{sat} is the soil hydraulic conductivity at saturation; f_{ice} is the fraction of ice to soil pore volume and it is calculated as:

$$f_{ice} = \left[1 - \min \left(1, \frac{\theta_{ice}}{\theta_{sat}} \right) \right]^2 \quad (B13)$$

References

- Baltzer, J.L., Veness, T., Chasmer, L.E., Sniderhan, A.E., Quinton, W.L., 2014. Forests on thawing permafrost: fragmentation, edge effects, and net forest loss. *Glob. Chang. Biol.* 20, 824–834. <https://doi.org/10.1111/gcb.12349>.
- Bao, T., Xu, X., Jia, G., Billesbach, D.P., Sullivan, R.C., 2021. Much stronger tundra methane emissions during autumn freeze than spring thaw. *Glob. Chang. Biol.* 27, 376–387. <https://doi.org/10.1111/gcb.15421>.
- Barman, R., Jain, A.K., 2016. Comparison of effects of cold-region soil/snow processes and the uncertainties from model forcing data on permafrost physical characteristics. *J. Adv. Model. Ear. Syst.* 8, 453–466. <https://doi.org/10.1002/2015MS000504>.
- Brown, J., Ferrians, O., Heginbottom, J.A., Melnikov, E., 2002. Circum-arctic Map of Permafrost and Ground-Ice conditions. Version 2. Boulder, Colorado. NSIDC Natl. Snow Ice Data Cent, USA. <https://doi.org/10.7265/skgb-kf16>.
- Cao, B., Gruber, S., Zheng, D., Li, X., 2020. The era5-land soil-temperature bias in permafrost regions. *Cryosph.* 14, 2581–2595. <https://doi.org/10.5194/tc-2020-76>.
- Chang, X., Jin, H., Zhang, Y., He, R., Luo, D., Wang, Y., Lü, L., Zhang, Q., 2015. Thermal impacts of boreal forest vegetation on active layer and permafrost soils in northern da xing'anling (hinggan) mountains, northeast china. *Arct., Antarct. Alp. Res.* 47, 267–279. <https://doi.org/10.1657/AAAR00C-14-016>.
- Chaudhary, N., Westermann, S., Lamba, S., Shurpali, N., Sannel, A.B.K., Schurgers, G., Miller, P.A., Smith, B., 2020. Modelling past and future peatland carbon dynamics across the pan-arctic. *Glob. Chang. Biol.* 26, 4119–4133. <https://doi.org/10.1111/gcb.15099>.
- Che, T., Li, X., Jin, R., Armstrong, R., Zhang, T., 2008. Snow depth derived from passive microwave remote-sensing data in china. *Ann. Glaciol.* 49, 145–154. <https://doi.org/10.3189/172756408787814690>.
- Chen, B., Chen, J.M., Baldocchi, D.D., Liu, Y., Wang, S., Zheng, T., Black, T.A., Croft, H., 2019. Including soil water stress in process-based ecosystem models by scaling down maximum carboxylation rate using accumulated soil water deficit. *Agric. For. Meteorol.* 276–277. <https://doi.org/10.1016/j.agrformet.2019.107649>, 107649.
- Chen, B., Chen, J.M., Ju, W., 2007. Remote sensing-based ecosystem-atmosphere simulation scheme (eass)-model formulation and test with multiple-year data. *Ecol. Model.* 209, 277–300. <https://doi.org/10.1016/j.ecolmodel.2007.06.032>.
- Chen, B., Li, J., 2008. Characteristics of spatial and temporal variation of seasonal and short-term frozen soil in china in recent 50 years. *Chines. J. Atmos. Sci.* 32, 432–443, 10.3878/j.issn.1006-9895.2008.03.02. (In Chinese with English Abstract).
- Chen, B., Liu, J., Chen, J.M., Croft, H., Gonsamo, A., He, L., Luo, X., 2016. Assessment of forest clumping effects on evapotranspiration estimates in forested ecosystems. *Agric. For. Meteorol.* 216, 82–92. <https://doi.org/10.1016/j.agrformet.2015.09.017>.
- Chen, J.M., Ju, W., Ciais, P., Viovy, N., Liu, R., Liu, Y., Lu, X., 2019. Vegetation structural change since 1981 significantly enhanced the terrestrial carbon sink. *Nat. Commun.* 10, 4–10. <https://doi.org/10.1038/s41467-019-12257-8>.
- Chen, L., Chen, Z., Jia, G., Zhou, J., Zhao, J., Zhang, Z., 2020. Influences of forest cover on soil freeze-thaw dynamics and greenhouse gas emissions through the regulation of snow regimes: a comparison study of the farmland and forest plantation. *Sci. Tot. Environ.* <https://doi.org/10.1016/j.scitotenv.2020.138403>.
- Clapp, R.B., Hornberger, G.M., 1978. Empirical equations for some soil hydraulic properties. *Wat. Resour. Res.* 14, 601–604. <https://doi.org/10.1029/WR014i004p00601>.
- de Vries, D.A., 1963. Thermal properties of soils. *Phys. Plant Environ.* 12, 33–46.
- Dong, G., Guo, J., Chen, J., Sun, G., Gao, S., Hu, L., Wang, Y., 2011. Effects of spring drought on carbon sequestration, evapotranspiration and water use efficiency in the songnen meadow steppe in northeast china. *Ecohydrol.* 4, 211–224. <https://doi.org/10.1002/eco.200>.
- Farouki, O.T., 1981. Thermal Properties of soils, CRREL monograph. U.S. Army Corps of Engineers. Cold Regions Research and Engineering Laboratory.
- Foster, A.C., Armstrong, A.H., Shuman, J.K., Shugart, H.H., Rogers, B.M., Mack, M.C., Goetz, S.J., Ranson, K.J., 2019. Importance of tree- and species-level interactions with wildfire, climate, and soils in interior alaska: implications for forest change under a warming climate. *Ecol. Model.* 409, 108765 <https://doi.org/10.1016/j.ecolmodel.2019.108765>.
- Frazer, G.W., Fournier, R.A., Trofymow, J.A., Hall, R.J., 2001. A comparison of digital and film fisheye photography for analysis of forest canopy structure and gap light transmission. *Agric. For. Meteorol.* 109, 249–263. [https://doi.org/10.1016/S0168-1923\(01\)00274-X](https://doi.org/10.1016/S0168-1923(01)00274-X).
- French, H.M., 2007. Permafrost, in: the periglacial environment. Wiley 83–115. <https://doi.org/10.1002/9781118684931>.
- Grosse, G., Goetz, S., McGuire, A.D., Romanovsky, V.E., Schuur, E.A.G., 2016. Changing permafrost in a warming world and feedbacks to the earth system. *Environ. Res. Lett.* 11, 040201 <https://doi.org/10.1088/1748-9326/11/4/040201>.
- Guan, D., Wu, J., Zhao, X., Han, S., Yu, G., Sun, X., Jin, C., 2006. CO₂ fluxes over an old, temperate mixed forest in northeastern china. *Agric. For. Meteorol.* 137, 138–149. <https://doi.org/10.1016/j.agrformet.2006.02.003>.
- Guo, D., Wang, H., 2014. Simulated change in the near-surface soil freeze/thaw cycle on the tibetan plateau from 1981 to 2010. *Chines. Sci. Bull.* 59, 2439–2448. <https://doi.org/10.1007/s11434-014-0347-x>.
- Guo, W., Liu, H., Anenkhonov, O.A., Shangguan, H., Sandanov, D.V., Korolyuk, A.Y., Hu, G., Wu, X., 2018. Vegetation can strongly regulate permafrost degradation at its southern edge through changing surface freeze-thaw processes. *Agric. For. Meteorol.* 252, 10–17. <https://doi.org/10.1016/j.agrformet.2018.01.010>.
- He, L., Chen, J.M., Pisek, J., Schaaf, C.B., Strahler, A.H., 2012. Global clumping index map derived from the modis brdf product. *Rem. Sens. Environ.* 119, 118–130. <https://doi.org/10.1016/j.rse.2011.12.008>.
- Helfricht, K., Hartl, L., Koch, R., Marty, C., Olefs, M., 2018. Obtaining sub-daily new snow density from automated measurements in high mountain regions. *Hydrol. Earth Syst. Sci.* 22, 2655–2668. <https://doi.org/10.5194/hess-22-2655-2018>.
- Hengl, T., Mendes de Jesus, J., Heuvelink, G.B.M., Ruípeirrez González, M., Kilibarda, M., Blagotić, A., Shangguan, W., Wright, M.N., Geng, X., Bauer-Marschallinger, B., Guevara, M.A., Vargas, R., MacMillan, R.A., Batjes, N.H., Leenaars, J.G.B., Ribeiro, E., Wheeler, I., Mantel, S., Kempen, B., 2017. SoilGrids250m: global gridded soil information based on machine learning. *PLoS ONE* 12, e0169748. <https://doi.org/10.1371/journal.pone.0169748>.
- Hollesen, J., Elberling, B., Jansson, P.E., 2011. Future active layer dynamics and carbon dioxide production from thawing permafrost layers in Northeast Greenland. *Glob. Chang. Biol.* 17, 911–926. <https://doi.org/10.1111/j.1365-2486.2010.02256.x>.
- Hu, G., Liu, H., Anenkhonov, O.A., Korolyuk, A.Y., Sandanov, D.V., Guo, D., 2013. Forest buffers soil temperature and postpones soil thaw as indicated by a three-year large-scale soil temperature monitoring in the forest-steppe ecotone in inner asia. *Glob. Planet. Change* 104, 1–6. <https://doi.org/10.1016/j.gloplacha.2013.02.002>.
- Hu, G., Zhao, L., Li, R., Wu, X., Wu, T., Xie, C., Zhu, X., Hao, J., 2020a. Thermal properties of active layer in permafrost regions with different vegetation types on the qinghai-tibetan plateau. *Theor. Appl. Climatol.* 139, 983–993. <https://doi.org/10.1007/s00704-019-03008-2>.
- Hu, G., Zhao, L., Zhu, X., Wu, X., Wu, T., Li, R., Xie, C., Hao, J., 2020b. Review of algorithms and parameterizations to determine unfrozen water content in frozen soil. *Geoderma* 368, 114277 <https://doi.org/10.1016/j.geoderma.2020.114277>.
- Jan, A., Coon, E.T., Painter, S.L., 2020. Evaluating integrated surface/subsurface permafrost thermal hydrology models in ats (v0.88) against observations from a polygonal tundra site. *Geosci. Model Dev.* 13, 2259–2276. <https://doi.org/10.5194/gmd-13-2259-2020>.
- Jin, X., Jin, H., Ihwana, G., Marchenko, S.S., Luo, D., Li, X., Liang, S., 2020. Impacts of climate-induced permafrost degradation on vegetation: a review. *Adv. Clim. Chang. Res.* <https://doi.org/10.1016/j.accre.2020.07.002>.
- Ju, W., Chen, J.M., Black, T.A., Barr, A.G., Liu, J., Chen, B., 2006. Modelling multi-year coupled carbon and water fluxes in a boreal aspen forest. *Agric. For. Meteorol.* 140, 136–151. <https://doi.org/10.1016/j.agrformet.2006.08.008>.
- Karjalainen, O., Luoto, M., Aalto, J., Hjort, J., 2019. New insights into the environmental factors controlling the ground thermal regime across the northern hemisphere: a comparison between permafrost and non-permafrost areas. *Cryosph.* 13, 693–707. <https://doi.org/10.5194/tc-13-693-2019>.
- Kim, Y., Kimball, J.S., Didan, K., Henebry, G.M., 2014. Response of vegetation growth and productivity to spring climate indicators in the conterminous united states derived from satellite remote sensing data fusion. *Agric. For. Meteorol.* 194, 132–143. <https://doi.org/10.1016/j.agrformet.2014.04.001>.
- Kim, Y., Still, C.J., Hanson, C.V., Kwon, H., Greer, B.T., Law, B.E., 2016. Canopy skin temperature variations in relation to climate, soil temperature, and carbon flux at a ponderosa pine forest in central Oregon. *Agric. For. Meteorol.* 226–227. <https://doi.org/10.1016/j.agrformet.2016.06.001>, 161–173.
- Kobayashi, T., Tateishi, R., Alsaaideh, B., Sharma, R.C., Wakaizumi, T., Miyamoto, D., Bai, X., Long, B.D., Gegentana, G., Maitinayazi, A., Cahyana, D., Häiretti, A., Morifushi, Y., Abake, G., Pratama, R., Zhang, N., Alifu, Z., Shirahata, T., Mi, L., Iizuka, K., Yusupujiang, A., Rinawan, F.R., Bhattachari, R., Phong, D.X., 2017. Production of global land cover data – glcnmo2013. *J. Geogr. Geol.* 9, 1. <https://doi.org/10.5539/jgg.v9n3p1>.
- Kumar, P., Kaleita, A.L., 2003. Assimilation of near-surface temperature using extended kalman filter. *Adv. Wat. Resour.* 26, 79–93. [https://doi.org/10.1016/S0309-1708\(02\)00098-2](https://doi.org/10.1016/S0309-1708(02)00098-2).
- Lawrence, D.M., Slater, A.G., 2008. Incorporating organic soil into a global climate model. *Clim. Dyn.* 30, 145–160. <https://doi.org/10.1007/s00382-007-0278-1>.
- Letts, M.G., Roulet, N.T., Comer, N.T., Skarupa, M.R., Verseghy, D.L., 2000. Parametrization of peatland hydraulic properties for the canadian land surface scheme. *Atmos. Ocean* 38, 141–160. <https://doi.org/10.1080/07055900.2000.964963>.

- Li, S., Asanuma, J., Eugster, W., Kotani, A., Liu, J.-J., Urano, T., Oikawa, T., Davaa, G., Oyunbaatar, D., Sugita, M., 2005a. Net ecosystem carbon dioxide exchange over grazed steppe in central mongolia. *Glob. Chang. Biol.* 11, 1941–1955. <https://doi.org/10.1111/j.1365-2486.2005.01047.x>.
- Li, S., Asanuma, J., Kotani, A., Eugster, W., Davaa, G., Oyunbaatar, D., Sugita, M., 2005b. Year-round measurements of net ecosystem co₂ flux over a montane larch forest in mongolia. *J. Geophys. Res. Atmos.* 110 <https://doi.org/10.1029/2004JD005453>. D09303.
- Li, S., Eugster, W., Asanuma, J., Kotani, A., Davaa, G., Oyunbaatar, D., Sugita, M., 2008. Response of gross ecosystem productivity, light use efficiency, and water use efficiency of mongolian steppe to seasonal variations in soil moisture. *J. Geophys. Res. Biogeosci.* 113 <https://doi.org/10.1029/2006JG000349>. G01019.
- Li, S., Eugster, W., Asanuma, J., Kotani, A., Davaa, G., Oyunbaatar, D., Sugita, M., 2006. Energy partitioning and its biophysical controls above a grazing steppe in central mongolia. *Agric. For. Meteorol.* 137, 89–106. <https://doi.org/10.1016/j.agrformet.2006.03.010>.
- Liu, J., Chen, J.M., Cihlar, J., Park, W.M., 1997. A process-based boreal ecosystem productivity simulator using remote sensing inputs. *Rem. Sens. Environ.* 62, 158–175. [https://doi.org/10.1016/S0034-4257\(97\)00089-8](https://doi.org/10.1016/S0034-4257(97)00089-8).
- Liu, Y., Liu, R., Chen, J.M., 2012. Retrospective retrieval of long-term consistent global leaf area index (1981–2011) from combined avhrr and modis data. *J. Geophys. Res. Biogeosci.* 117 <https://doi.org/10.1029/2012JG002084>. G04003.
- Nitzbon, J., Westermann, S., Langer, M., Martin, L.C.P., Strauss, J., Laboor, S., Boike, J., 2020. Fast response of cold ice-rich permafrost in northeast siberia to a warming climate. *Nat. Commun.* 11, 1–12. <https://doi.org/10.1038/s41467-020-15725-8>.
- Niu, G., Yang, Z., 2006. Effects of frozen soil on snowmelt runoff and soil water storage at a continental scale. *J. Hydrometeorol.* 7, 937–952. <https://doi.org/10.1175/JHM538.1>.
- Novara, A., Rühl, J., La Mantia, T., Gristina, L., La Bella, S., Tuttolomondo, T., 2015. Litter contribution to soil organic carbon in the processes of agriculture abandon. *Solid Ear.* 6, 425–432. <https://doi.org/10.5194/se-6-425-2015>.
- Pachauri, R.K., Allen, M.R., Barros, V.R., Broome, J., Cramer, W., Christ, R., Church, J.A., Clarke, L., Dahe, Q., Dasgupta, P., 2014. Climate change 2014: synthesis report. In: Contribution of Working Groups I, II and III to the Fifth Assessment Report of the Intergovernmental Panel On Climate Change, Intergovernmental Panel On Climate Change. Geneva, Switzerland. 10.1111/j.1728-4457.2001.00203.x.
- Schädel, C., Bader, M.K.F., Schuur, E.A.G., Biasi, C., Bracho, R., Capek, P., De Baets, S., Diaková, K., Ernakovich, J., Estop-Aragones, C., Graham, D.E., Hartley, I.P., Iversen, C.M., Kane, E., Knoblauch, C., Lupascu, M., Martikainen, P.J., Natali, S.M., Norby, R.J., O'Donnell, J.A., Chowdhury, T.R., Santrucková, H., Shaver, G., Sloan, V. L., Treat, C.C., Turetsky, M.R., Waldro, M.P., Wickland, K.P., 2016. Potential carbon emissions dominated by carbon dioxide from thawed permafrost soils. *Nat. Clim. Chang.* 6, 950–953. <https://doi.org/10.1038/nclimate3054>.
- Tao, J., Reichle, R.H., Koster, R.D., Forman, B.A., Xue, Y., 2017. Evaluation and enhancement of permafrost modeling with the nasa catchment land surface model. *J. Adv. Model. Ear. Syst.* 9, 2771–2795. <https://doi.org/10.1002/2017MS001019>.
- Tian, Y., Zhang, Q., Liu, X., Meng, M., 2018. Stem radius variation in response to hydro-thermal factors in larch. *For.* 9, 602. <https://doi.org/10.3390/f9100602>.
- Tian, Z., Lu, Y., Horton, R., Ren, T., 2016. A simplified de Vries-based model to estimate thermal conductivity of unfrozen and frozen soil. *Eur. J. Soil Sci.* 67, 564–572. <https://doi.org/10.1111/ejss.12366>.
- Wang, Q., Lv, W., Li, B., Zhou, Y., Jiang, L., Piao, S., Wang, Y., Zhang, L., Meng, F., Liu, P., Hong, H., Li, Y., Dorji, T., Luo, C., Zhang, Z., Ciais, P., Penuelas, J., Kardol, P., Zhou, H., Wang, S., 2020. Annual ecosystem respiration is resistant to changes in freeze-thaw periods in semi-arid permafrost. *Glob. Chang. Biol.* 26, 2630–2641. <https://doi.org/10.1111/gcb.14979>.
- Wang, S., Chen, W., Cihlar, J., 2002. New calculation methods of diurnal distribution of solar radiation and its interception by canopy over complex terrain. *Ecol. Modell.* 155, 191–204. [https://doi.org/10.1016/S0304-3800\(02\)00122-9](https://doi.org/10.1016/S0304-3800(02)00122-9).
- Wei, Z., Jin, H., Zhang, J., Yu, S., Han, X., Ji, Y., He, R., Chang, X., 2011. Prediction of permafrost changes in northeastern china under a changing climate. *Sci. China Earth Sci.* 54, 924–935. <https://doi.org/10.1007/s11430-010-4109-6>.
- Wu, X., Liu, H., Li, X., Liang, E., Beck, P.S.A., Huang, Y., 2016. Seasonal divergence in the interannual responses of northern hemisphere vegetation activity to variations in diurnal climate. *Sci. Rep.* 6 <https://doi.org/10.1038/srep19000>, 19000.
- Yoshikawa, K., Úbeda, J., Masías, P., Pari, W., Apaza, F., Vasquez, P., Ccallata, B., Concha, R., Luna, G., Iparraguirre, J., Ramos, I., De la Cruz, G., Cruz, R., Peláez, R., Bonshoms, M., 2020. Current thermal state of permafrost in the southern peruvian andes and potential impact from el niño–southern oscillation (enso). *permafrost periglac. Proc.* 1–12. <https://doi.org/10.1002/ppg.2064>.
- Yue, Y., Liu, H., Xue, J., Li, Y., Guo, W., 2020. Ecological indicators of near-surface permafrost habitat at the southern margin of the boreal forest in china. *Ecol. Indic.* 108, 105714 <https://doi.org/10.1016/j.ecolind.2019.105714>.
- Zhang, L., Mao, J., Shi, X., Ricciuto, D., He, H., Thornton, P., Yu, G., Li, P., Liu, M., Ren, X., Han, S., Li, Y., Yan, J., Hao, Y., Wang, H., 2016. Evaluation of the community land model simulated carbon and water fluxes against observations over chinaflux sites. *Agric. For. Meteorol.* 226–227. <https://doi.org/10.1016/j.agrformet.2016.05.018>, 174–185.
- Zhang, S., Zhang, J., Bai, Y., Koju, U.A., Igbawua, T., Chang, Q., Zhang, D., Yao, F., 2018. Evaluation and improvement of the daily boreal ecosystem productivity simulator in simulating gross primary productivity at 41 flux sites across Europe. *Ecol. Modell.* 368, 205–232. <https://doi.org/10.1016/j.ecolmodel.2017.11.023>.
- Zhang, T., 2005. Influence of the seasonal snow cover on the ground thermal regime: an overview. *Rev. Geophys.* 43 <https://doi.org/10.1029/2004RG000157>. RG4002.
- Zhang, X., Liu, X., Zhang, Q., Zeng, X., Xu, G., Wu, G., Wang, W., 2018. Species-specific tree growth and intrinsic water-use efficiency of dahurian larch (*larch gmelini*) and mongolian pine (*pinus sylvestris* var. *mongolica*) growing in a boreal permafrost region of the greater hinggan mountains, northeastern China. *Agric. For. Meteorol.* 248, 145–155. <https://doi.org/10.1016/j.agrformet.2017.09.013>.
- Zhang, Y., Carey, S.K., Quinton, W.L., 2008. Evaluation of the algorithms and parameterizations for ground thawing and freezing simulation in permafrost regions. *J. Geophys. Res. Atmos.* 113, 1–17. <https://doi.org/10.1029/2007JD009343>.